Journal of the Brazilian Society of Mechanical Sciences and Engineering (2022) 44:378
https://doi.org/10.1007/s40430-022-03690-w

TECHNICAL PAPER

Simulation of airfoil dynamic stall suppression with a burst control blade in a transitional flow regime

Erfan Salimipour[1] · Shima Yazdani[1] · Mehdi Ghalambaz[2,3]

Received: 25 January 2022 / Accepted: 13 July 2022 / Published online: 3 August 2022

Abstract
The present study numerically analyzed the effect of a passive flow control method to suppress the dynamic stall phenomenon on a NACA 0012 airfoil exposed to a uniform free flow at the transitional Reynolds number of 1.3×10^5. A thin blade was mounted on the airfoil's leading edge to control the separation bubble burst. The fluid relations of motion are the unsteady Reynolds-Averaged Navier–Stokes equations, solved implicitly by a second-order finite-volume solver. A three-equation transitional turbulence model with the capability of separation bubble prediction was used. Numerical results for several pressure distributions and aerodynamic coefficients were compared with available experimental results. The agreement was fair, confirming the reliability of the utilized computational method in the stall conditions. Results from the current work demonstrated that the control blade could prevent the separation bubble burst leading to a reduction in the static and dynamic stall effects. The blade caused a delay in the onset of the flow separation and improved the lift and drag coefficients, particularly in the pitch down motion of the airfoil. For the attack angle range between 5° and 15°, a significant dynamic stall control was observed, while at a wider range, the blade effect was low. The dynamic stall is a significant phenomenon resulting in a blade vibration due to the aeroelastic or hydrodynamic effects. The dynamic stall can lead to the flutter phenomenon that may cause the structure to break.

Keywords Numerical simulation · Transitional flow · Dynamic stall · Control blade · Navier–Stokes equations

1 Introduction

Airfoils exposed to low Reynolds number flows are used in various applications such as medium and small-size wind turbines and micro-aero vehicles. There is a laminar separation from the suction surface for low Reynolds airfoils, and the flow quickly reattaches to the surface. The area between the separated flow and the reattachment point is defined as a Laminar Separation Bubble (LSB) [35] . Laminar separation bubbles lead to efficiency reduction in aerodynamic systems operating at low Reynolds numbers ($\mathrm{Re} < 7 \times 10^5$) [8]. Depending on the correction of the corresponding pressure distribution, LSB can be long or short [32]. Fluctuations in flow parameters could cause the bubble to pass from short to long abruptly, known as the bubble bursting [34] .

The LSB occurrence can lead to unpleasant matters, such as increasing the drag and sudden decrease in the airfoil lift owing to the burst of the bubbles [42]. The bubble size decreases by increasing the attack angle (α) until the bubble burst occurs, causing the full separation [30]. Airfoil stall categorizes into three groups, including the trailing edge stall, leading edge stall, and thin airfoil stall. The LSB is grouped as a leading edge stall and thin airfoil stall [5]. Marxen and Henningson [19] investigated the relationship between bubble bursting and airfoil stall. Their results showed that the bubble bursts when the disturbances could not reattach the flow. Another study was conducted by Alferez et al. [4] to find a mechanism by which the LSB bursting occurred and caused the stall.

Various engineering applications may experience dynamic stall, such as wind turbines and aircraft

Technical Editor: André Cavalieri.

✉ Mehdi Ghalambaz
mehdighalambaz@duytan.edu.vn

[1] Department of Mechanical Engineering, Quchan University of Technology, Quchan, Iran

[2] Institute of Research and Development, Duy Tan University, Da Nang 550000, Vietnam

[3] Faculty of Electrical – Electronic Engineering, Duy Tan University, Da Nang 550000, Vietnam

maneuvering. When an airfoil oscillates through the static stall angle, a dynamic stall phenomenon can be formed, which leads to the formation of the hysteresis loops of the lift and drag coefficients [3]. According to [36], the dynamic stall is typically accompanied by the presence of an LSB near the leading edge of a constant pitching rate motion. The negative effects of dynamic stall usually appear in the pitch down motion of the airfoil. In cases of severe aerodynamic instability due to the dynamic stall, a significant disturbance in the effective angle of attack can cause substantial deviations from the nominally steady flight [7]. There have been several comprehensive reviews of this phenomenon, including works by McCroskey [20], Carr [9], Visbal and Garmann [37], and Miotto et al. [20].

Knowledge of the dynamic stall has been complicated due to the highly unsteady nature of flow fields and the flow's reliance on interrelated factors like flow stream conditions, aircraft geometry, and wing movement. Dynamic stall flows exhibit challenging fluid phenomena such as boundary layer separation, transition, layer instability, and LSB bursts depending on the system parameters [38]. Numerical and experimental research has shed light on dynamic stall regimes, their unsteady flow structure, and their induced transient aerodynamic loads. Computational studies have been carried out using several techniques, including two-dimensional laminar simulations [10], three-dimensional transitional simulations [12], and Reynolds-averaged Navier–Stokes (RANS) calculations using a hierarchy of turbulence models [11]. Using an appropriate transitional model could partially correct the shortcomings of the Reynolds-averaged approaches [15, 36]. In the past, turbulence models were one or two-equation; today, with the development of turbulence models and the introduction of three-equation models such k-k_L-ω, the RANS methods have been improved [21].

In order to control the flow and improve the airfoil aerodynamic characteristics, two common types of active and passive flow control methods are used. Significant changes can be observed in the aerodynamic parameters using active flow control methods such as suction, blowing, artificial jet, and co-flow jet. However, active methods have shortcomings, such as safety concerns, high maintenance cost, and high energy consumption. Salimipour and Yazdani [29] placed a moving surface as an active control mechanism on the suction surface of the S809 airfoil to improve its aerodynamic performance. Their results showed a great improvement in the aerodynamic coefficients. Furthermore, Bak Khoshnevis et al. [6] used another active flow control, a so-called co-flow jet, on different symmetric airfoils to investigate the airfoil thickness effect on the co-flow jet performance in a transitional flow regime. They concluded that the co-flow jet had a better performance on the thick airfoils. In addition, Salimipour and Salimipour [28] created a moving wall on the upper and lower surfaces of a cylinder to reduce the drag coefficient and power consumption. Abdelraouf et al. [2] numerically investigated the different models of plasma actuators to suppress the flow separation on the NACA 0012 airfoil for an attack angle range between 0° and 20°.

Passive flow control methods such as using a blade, slot, geometry change, and surface roughness are essential methods because no additional cost is spent in terms of energy consumption. Some aspects of flow over airfoils have been investigated in recent studies [14, 22, 25]. Patial et al. [23] performed a numerical study to investigate the cavity effect on the flow past a Selig-Donovan 7003 and a NACA 0012 airfoil at the Reynolds number of 10^5. They concluded that the cavity improved the aerodynamic parameters; however, the cavity specifications are different for each airfoil. Wang et al. [41] numerically investigated the impact of a vortex generator on a wind turbine airfoil. They concluded that the vortex generators could improve the aerodynamic performance of the airfoil. Furthermore, Wang et al. [40] used a slat on the S809 airfoil's leading edge and studied the aerodynamic characteristics of the airfoil. The slat could well suppress the flow separation.

Magill et al. [18] used a pulsed vortex generator jet to delay the dynamic stall on a pitching airfoil at the Reynolds number of 1.7×10^5. Abbasi and Yazdani [1] numerically evaluated a synthetic jet's effect on the dynamic stall of a NACA 0015 airfoil. Khoshnevis et al. [16] utilized a co-flow jet on the NACA 0025 airfoil to investigate its effect on the static and dynamic stall control at different Reynolds numbers. He et al. [13] experimentally studied the effect of the trailing edge flap on the dynamic stall of a pitching NACA0015 airfoil.

Rinoie et al. [25] used a burst control plate for stall suppression on the leading edge of a stationary NACA 0012 airfoil. Their experimental data demonstrated that the burst control plate could delay the stall angle at an attack angle range from $\alpha = 0°$ to $\alpha = 15°$ and $\mathrm{Re} = 1.3 \times 10^5$. They performed their experiments in a wind tunnel with the turbulence intensity less than 0.16%. Since Rinoie et al. [25] focused on stationary stall suppression, the dynamic stall was not investigated. However, the dynamic stall could be significant when the aeroelastic or hydrodynamic effects cause a blade to vibrate. This can lead to the occurrence of the flutter phenomenon that may cause the structure to break.

The present research aims to investigate the control of the dynamic stall on a pitching NACA 0012 airfoil at $\mathrm{Re} = 1.3 \times 10^5$ via a burst control blade. It is a passive flow control technique that, in this study, has been applied for the first time to investigate the effects on the dynamic stall of transitional flows. For this purpose, a thin control blade with the height of 0.005 airfoil's chord is positioned normal to the airfoil surface at a distance of 0.07 chord from

the airfoil leading edge. Fig. 1 depicts the configuration of the blade on the airfoil's upper surface. The governing equations and the numerical solution method are presented in Sect. 2. The flow field is modeled using an appropriate turbulence model with LSB prediction capability associated with a transitional flow regime containing the laminar separation bubble in a moving coordinate system. Finally, the RANS equations are solved by developing an in-house Fortran code. Validation, grid study, and results are described in Sect. 3. Diagrams of lift and drag coefficients, streamlines, and turbulent kinetic energy contours are given to illustrate how the blade influences dynamic stall.

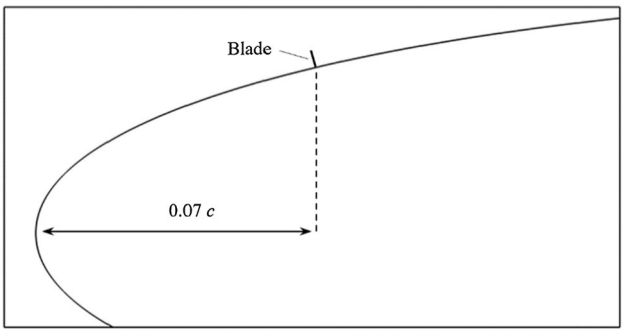

Fig. 1 Location of the blade on the leading edge

2 Mathematical and numerical formulation

The physical model considered in the present study consists of a rigid airfoil surrounded by a computational domain. Fig. 2 shows the extent of the computational domain along with the boundary conditions. For the dynamic stall problem, the airfoil makes a pitching motion about the quarter-chord from the leading edge. The implemented boundary conditions are a velocity inlet, pressure outlet, and solid boundaries depicted in the figure. It should be noted that the entire grid including the velocity inlet and pressure outlet boundary conditions is moving during the airfoil rotation. However, the boundary conditions are defined in such a way that their spatial position remains constant during the rotation. In fact, the position of the boundary conditions is corrected at each time step.

Since a moving coordinate system is used for the pitching airfoil simulation, it is necessary to include the coordinate system velocity in the governing equations. By assuming an unsteady, two-dimensional, incompressible, and viscous flow, the RANS equations for a moving coordinate system in the integral form are written as follows [31]:

$$\oint_{\partial\Omega} \rho V dS = 0 \tag{1}$$

$$\frac{\partial}{\partial t}\int_{\Omega} \vec{W} d\Omega + \oint_{\partial\Omega} \left(\vec{J} - V_t \vec{W}\right) dS = 0 \tag{2}$$

with the surface element dS, control volume Ω, control surface $\partial\Omega$, flow normal velocity V, normal velocity of the face

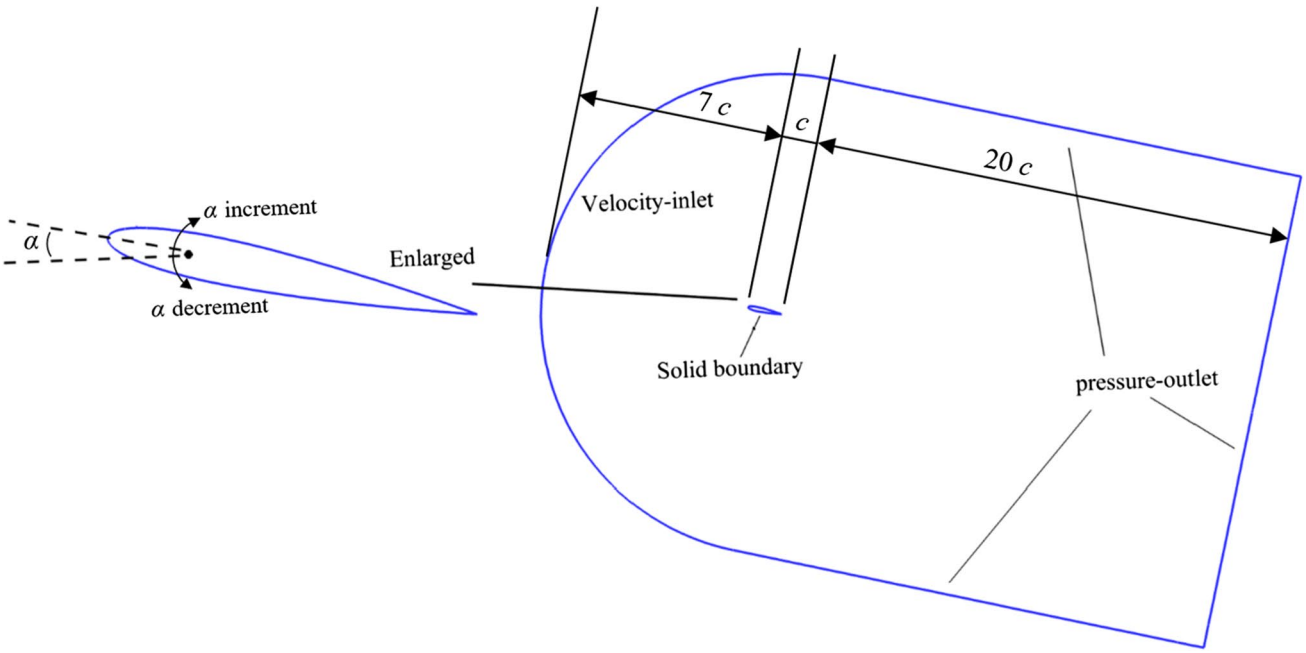

Fig. 2 Computational domain and boundary conditions

of the control volume V_t, vector of the conservative variables $\vec{W}$, and sum of the convection and diffusion fluxes $\vec{J}$, which are defined as follows:

$$\vec{W} = \begin{bmatrix} \rho u \\ \rho v \end{bmatrix}, \quad \vec{J} = \begin{bmatrix} \rho u V + n_x p - (\mu + \mu_t)\left(n_x \frac{\partial u}{\partial x} + n \frac{\partial u}{\partial y}\right) \\ \rho v V + n_y p - (\mu + \mu_t)\left(n_x \frac{\partial v}{\partial x} + n_y \frac{\partial v}{\partial y}\right) \end{bmatrix} \tag{3}$$

$$V = n_x u + n_y v \tag{4}$$

$$V_t = n_x dx/dt + n_y dy/dt \tag{5}$$

where u and v are the fluid velocities, and dx/dt and dy/dt denote the coordinate system velocities. p is the pressure and μ and μ_t are the dynamic and turbulent eddy viscosity, respectively. Furthermore, n_x and n_y are the components of the normal vectors on the control volume faces.

Numerical simulation of a transitional flow consisting of laminar separation bubble using RANS equations requires a turbulence model capable of detecting the bubble at the correct location within the transitional flow. In order to simulate the transitional-turbulent flow, the three-equation k-k_L-ω turbulence model proposed by Walters and Cokljat [39] is used. Furthermore, the revisions of the model proposed by Salimipour [27] are applied to simulate the laminar separation bubbles. The equations of the k-k_L-ω model are expressed as follows:

$$\frac{Dk_T}{Dt} = P_{k_T} + R_{BP} + R_{NAT} - \omega k_T - D_T + \frac{\partial}{\partial x_j}\left[\left(\nu + \frac{\alpha_T}{\sigma_k}\right)\frac{\partial k_T}{\partial x_j}\right] \tag{6}$$

$$\frac{Dk_L}{Dt} = P_{k_L} - R_{BP} - R_{NAT} - D_L + \frac{\partial}{\partial x_j}\left[\nu \frac{\partial k_L}{\partial x_j}\right] \tag{7}$$

$$\frac{D\omega}{Dt} = C_{\omega 1}\frac{\omega}{k_T}P_{k_T} + \left(\frac{C_{\omega R}}{f_W} - 1\right)\frac{\omega}{k_T}\left(R_{BP} + R_{NAT}\right) - f_W^2 C_{\omega 2}\omega^2 + C_{\omega 3} f_\omega \alpha_T f_W^2 \frac{\sqrt{k_T}}{d^3} + \frac{\partial}{\partial x_j}\left[\left(\nu + \frac{\alpha_T}{\sigma_\omega}\right)\frac{\partial \omega}{\partial x_j}\right] \tag{8}$$

where k_T, k_L, and ω are the turbulent kinetic energy, laminar kinetic energy, and specific dissipation rate, respectively. Moreover, P, R_{BP}, R_{NAT}, and D denote the turbulent production, bypass transition, natural transition, and near-wall dissipation, respectively. Closure equations related to the k-k_L-ω model are presented in [27]. As with other models in the k-ω family, this model does not require a wall function. For simulation of the viscous sublayer, the computational grid must have a sufficient density in the vicinity of the solid wall. The y^+ dimensionless parameter is an important parameter for determining the grid quality used to solve turbulent flow problems. In the employed model, the value of y^+ adjacent to the wall should be lower than one. Fig. 3 depicts the wall y^+ distribution of the bladed airfoil at $\alpha = 14°$ including the flow separation. As can be seen, the maximum value of y^+ reaches about 1.

An in-house incompressible flow solver based on a pressure-based scheme is utilized for the flow simulations utilized in [28, 29]. A second-order discretization of the momentum equations in time and space is implemented in the current solver. A 0.1% turbulence intensity is applied to the free-stream. The solver's characteristics outputs are the lift and drag coefficients. The pressure distribution and the streamlines are also the field outputs. Then, the following equations are used to evaluate the lift and drag coefficients:

$$C_p = \frac{p - p_\infty}{1/2 \rho U_\infty^2} \tag{9}$$

$$C_d = \frac{F_d}{1/2 \rho U_\infty^2 c} \tag{10}$$

$$C_l = \frac{F_l}{1/2 \rho U_\infty^2 c} \tag{11}$$

where F_l and F_d represent the drag and lift forces, and c indicates the airfoil chord length. Here, U_∞ and p_∞ denote the velocity and pressure of the free stream, respectively.

To study the dynamic stall phenomenon, a pitching motion is applied to the airfoil as the following equation:

$$\alpha(t) = \alpha_m + \alpha_0 \sin(\omega t) \tag{12}$$

where α_m and α_0 denote the mean attack angle and angular amplitude, respectively. The angular velocity ω is related to the reduced frequency defined as follows:

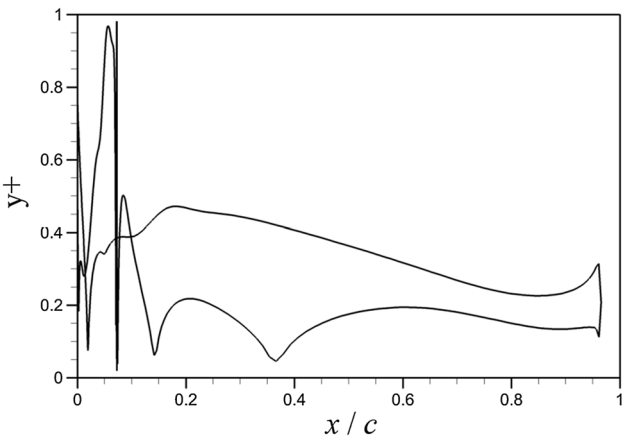

Fig. 3 y + distribution of the bladed airfoil's surface

$$k = \frac{\omega c}{2U_\infty} \tag{13}$$

A 730×90 and an 800×90 C-type grid with a relatively good orthogonality were used for the baseline and bladed airfoils, respectively. The number to the left of the multiplication sign denotes the grid points number in the peripheral direction, and the right number is the points number perpendicular to the airfoil surface. Fig. 4 depicts these two grids in a close-up view of the airfoils.

3 Results and discussion

3.1 Code validation and grid check

Before using the present computer code to simulate the static and dynamic stall suppressions, a code validation study is carried out in two problems of stationary and pitching airfoils. The pressure distribution coefficient for the NACA 0012 airfoil obtained by the present study and also the experimental data from (Rinoie, 2009) at $\alpha = 11°$, 12° and 13° and $\mathrm{Re} = 1.3 \times 10^5$ are shown in Fig. 5. A small difference between the present results and experimental data is observed; so that the maximum error at $\alpha = 11°$, 12°, and 13° is 8%, 12%, and 10%, respectively. Moreover, to check the grid independency, two solutions are performed with 530×70 and 330×55 grid point at $\alpha = 12°$, as shown in Fig. 5(b). It is seen that the pressure coefficients in the 730×90 and 530×70 grids are very similar, while the result of the 330×55 grid is very different. This has a separation bubble at $x / c = 0.55$ with more suction peak than that of the other grids. It can be concluded that an unsuitable grid cannot accurately model the turbulence features. A short separation bubble is formed at $\alpha = 11°$, while a long separation bubble is observed at $\alpha = 12°$, 13°. In fact, the bubble burst at $\alpha = 12°$ causes the stall onset at this angle of attack. Fig. 6 shows the streamlines and contours of the pressure coefficient for these two types of bubbles. The flow reattaches on the leading edge and trailing edge for the short and long bubbles, respectively.

Next cases examine the solver capability to simulate the flow around a pitching airfoil, including a dynamic stall. For this purpose, the hysteresis loops of the lift and drag coefficients of the pitching NACA 0012 airfoil in three cases are compared with the experimental data obtained by Lee and Gerontakos [17] at $\mathrm{Re} = 1.35 \times 10^5$. In the two first cases, the mean attack angle and oscillation amplitude are $\alpha_m = 10°$ and $\alpha_0 = 5°$, respectively. The reduced frequencies of oscillation are $k = 0.05$ and 0.1. In the third case, the mean attack angle, oscillation amplitude, and reduced frequency are $\alpha_m = 10°$, $\alpha_0 = 10°$, and $k = 0.1$, respectively. Fig. 7, 8 and 9 show the

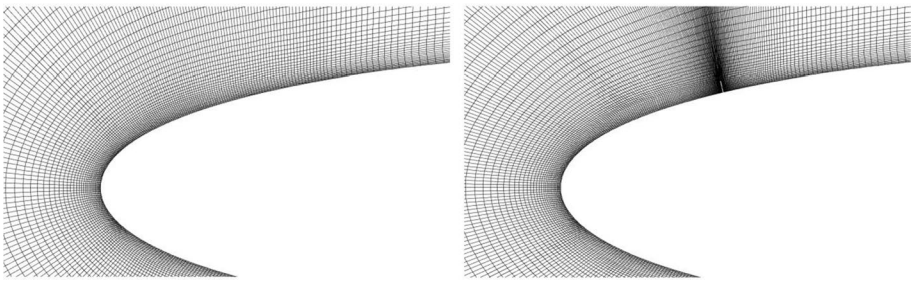

Fig. 4 C-type grids around the baseline and bladed NACA 0012 airfoils

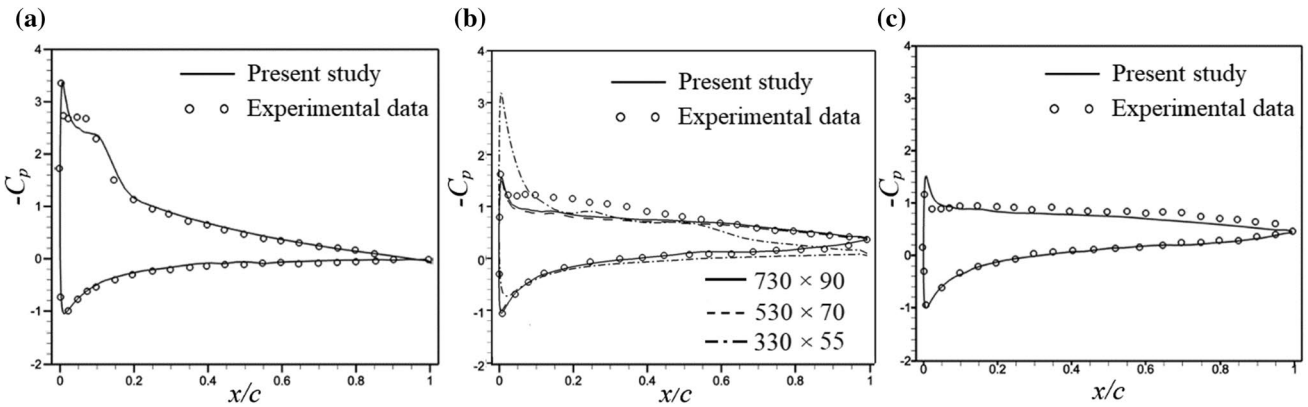

Fig. 5 Comparison of the pressure coefficients for NACA 0012 between the present results and experimental data from (Rinoie, 2009) at $\mathrm{Re} = 1.3 \times 10^5$, **a** $\alpha = 11°$, **b** $\alpha = 12°$, **c** $\alpha = 13°$

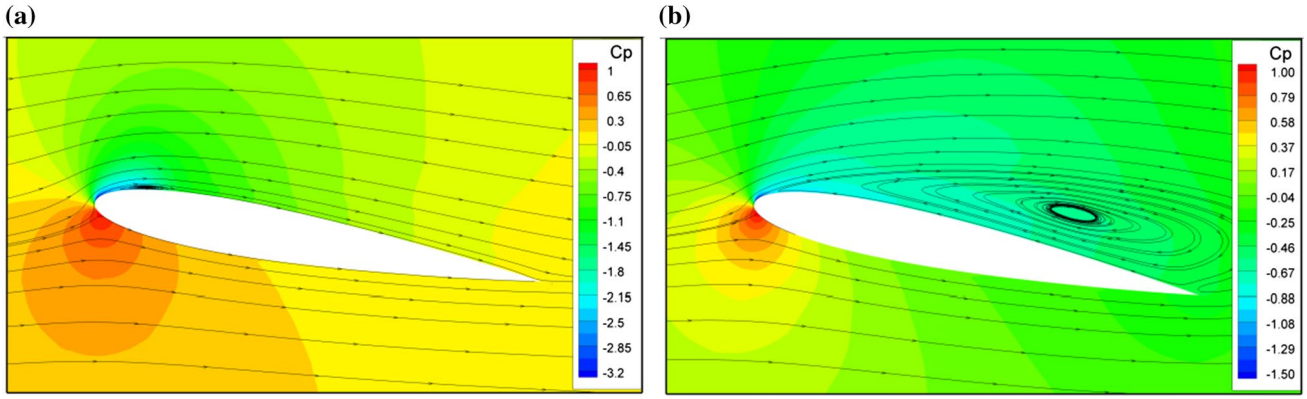

Fig. 6 Streamlines and contours of the pressure coefficient at **a** $\alpha = 11°$ and **b** $\alpha = 12°$

lift (C_l) and drag (C_d) coefficient hysteresis loops of the airfoil at the above-mentioned conditions. In the first case, the lift and drag coefficients are well simulated in both pitch up and pitch down motions of the airfoil. In the second case, the lift coefficient has a small difference with the experimental data at $\alpha = 15°$ and also in the pitch down motion for $12° \leq \alpha \leq 14°$. In the third case, the present results seem to be in a good correspondence with the experimental data except for predicting the lift coefficient at $\alpha = 20°$.

3.2 Bubble burst study for stationary airfoil

Before the investigation of the dynamic stall suppression, the effect of the bubble burst control blade on a stationary airfoil under the stalled and unstalled conditions is evaluated. In order to control the LSB burst, a thin blade is used, which is located normal to the airfoil surface near the leading edge. Airfoils in a transitional flow can experience the stall condition when a bubble forms near the leading edge, which grows to cover the entire suction surface of airfoil. For this reason, the blade must be located near the leading edge and before the bubble position. Under these circumstances, the blade creates a fluctuation in the flow, increasing Reynolds stresses and preventing bubble growth. The blade height should be such that it does not increase the drag force. On the other hand, it must be able to create enough fluctuation at the leading edge. The size of the short bubble (before bursting) can be used as a criterion for determining the blade height. This height is approximately 0.005 chord length.

Figure 10 depicts the pressure distribution coefficients of the baseline and bladed NACA 0012 airfoils at $\alpha = 11°$, 12°, and 13°. The pressure distribution at $\alpha = 11°$ has no

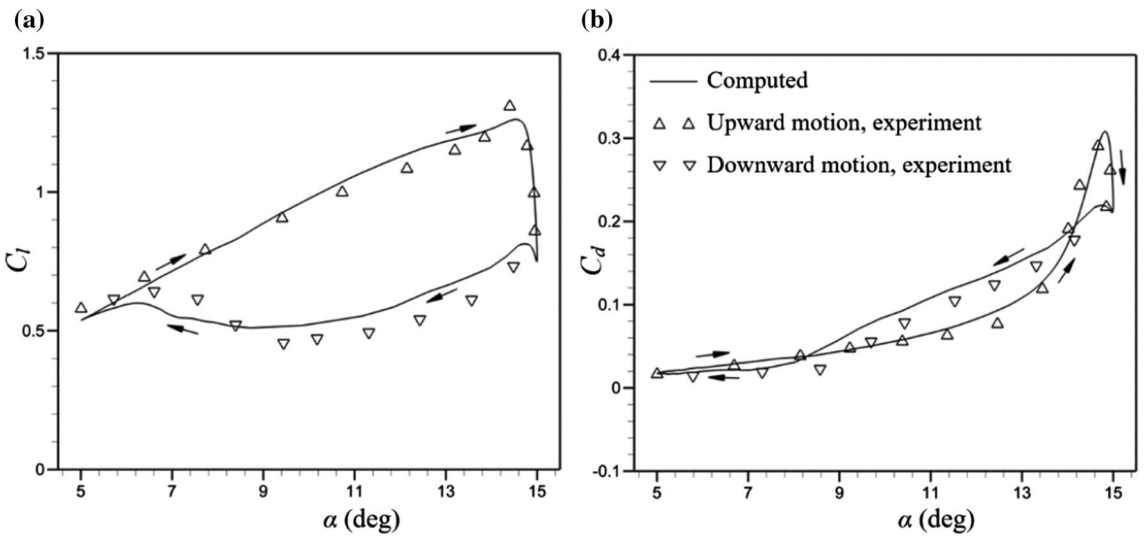

Fig. 7 Comparison of the lift and drag coefficient hysteresis loops with the experimental data from [17] at $\mathrm{Re} = 1.35 \times 10^5$, $\alpha_m = 10°$, $\alpha_0 = 5°$, $k = 0.05$, **a** C_l, **b** C_d

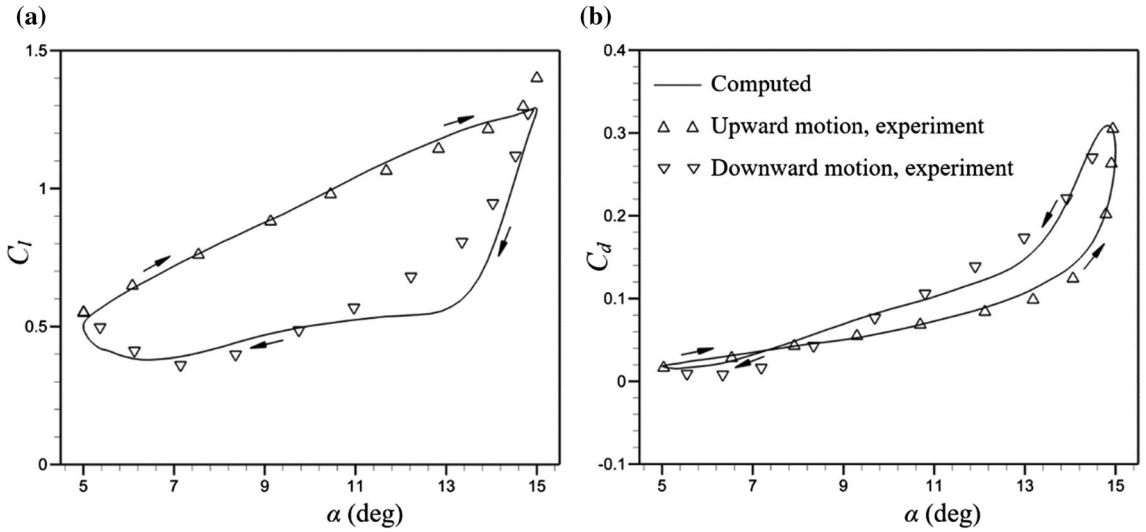

Fig. 8 Comparison of the lift and drag coefficient hysteresis loops with the experimental data from [17] at $\mathrm{Re}=1.35\times10^5$, $\alpha_m = 10^o$, $\alpha_0 = 5^o$, $k=0.1$, **a** C_l, **b** C_d

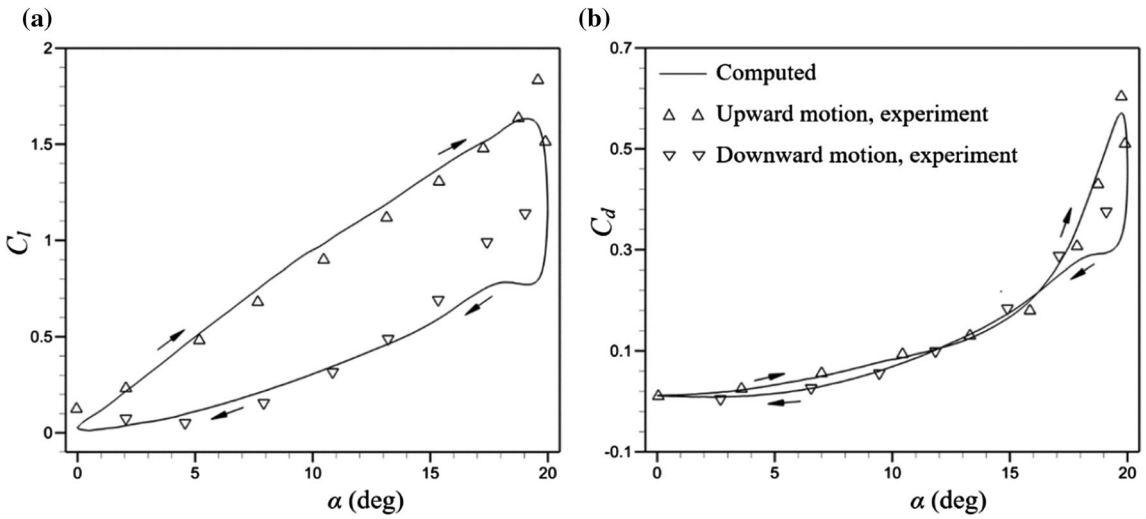

Fig. 9 Comparison of the lift and drag coefficient hysteresis loops with the experimental data from [17] at $\mathrm{Re}=1.35\times10^5$, $\alpha_m = 10^o$, $\alpha_0 = 10^o$, $k=0.1$, **a** C_l, **b** C_d

considerable difference between the baseline and bladed airfoils because the stall does not occur. In fact, the blade does not affect the short separation bubble. At $\alpha=12°$, the blade greatly controls the long separation bubble, and the structure of the short bubble is still preserved. The mechanism of the present blade's performance is similar to the effect of surface roughness. In fact, the blade causes sudden changes in the flow velocity. In this situation, the viscous force may not be sufficient to maintain the regular motion of the fluid particles in the laminar flow. As a result, the velocity fluctuation increases leading to mixing the fluid layers. This mixing creates a stronger kinetic energy than that of the laminar flow in the boundary layer, which is called turbulent kinetic energy. RANS equations generally models the Reynolds stresses as a function of turbulent viscosity. This quantity is proportional to the turbulent kinetic energy (TKE). In fact, the velocity fluctuations are the cause of TKE formation and TKE is the cause of turbulence viscosity. When the turbulent kinetic energy increases, the flow has more momentum to withstand the adverse pressure gradient. As a result, the growth of vortices is reduced.

At $\alpha=13°$, the blade fails to suppress the bubble bursting, and consequently, the stall occurs while the leading edge suction somewhat increases. Fig. 11 depicts the

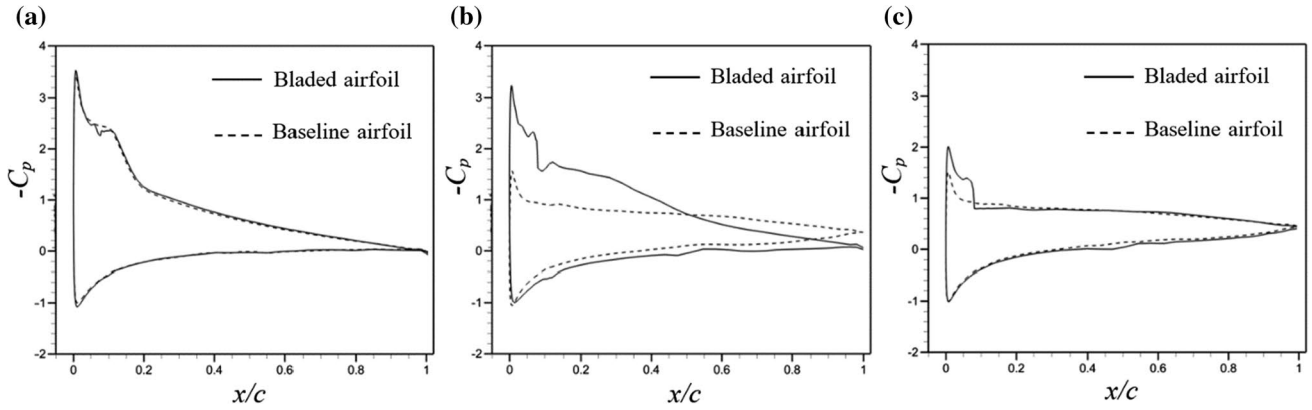

Fig. 10 Comparison of the pressure coefficients between the baseline and bladed NACA 0012 airfoils, (a) $\alpha = 11°$, (b) $\alpha = 12°$, **c** $\alpha = 13°$

streamlines along with the turbulent kinetic energy (TKE) contours for the baseline and bladed airfoils at $\alpha = 12°$.

An increase in the TKE near the control blade causes the reattachment of the flow. As can be seen, a short bubble exists behind the blade.

3.3 Dynamic stall suppression

In this section, the effect of the bubble burst control blade on the dynamic stall phenomenon is studied. For this purpose, the lift and drag hysteresis loops are drawn for the baseline and bladed NACA 0012 airfoils in five cases. The characteristics of the airfoil oscillation are presented in Table 1. Figs. 12, 13, 14, 15 and 16 show the comparison of the baseline and bladed airfoil results. In all the cases,

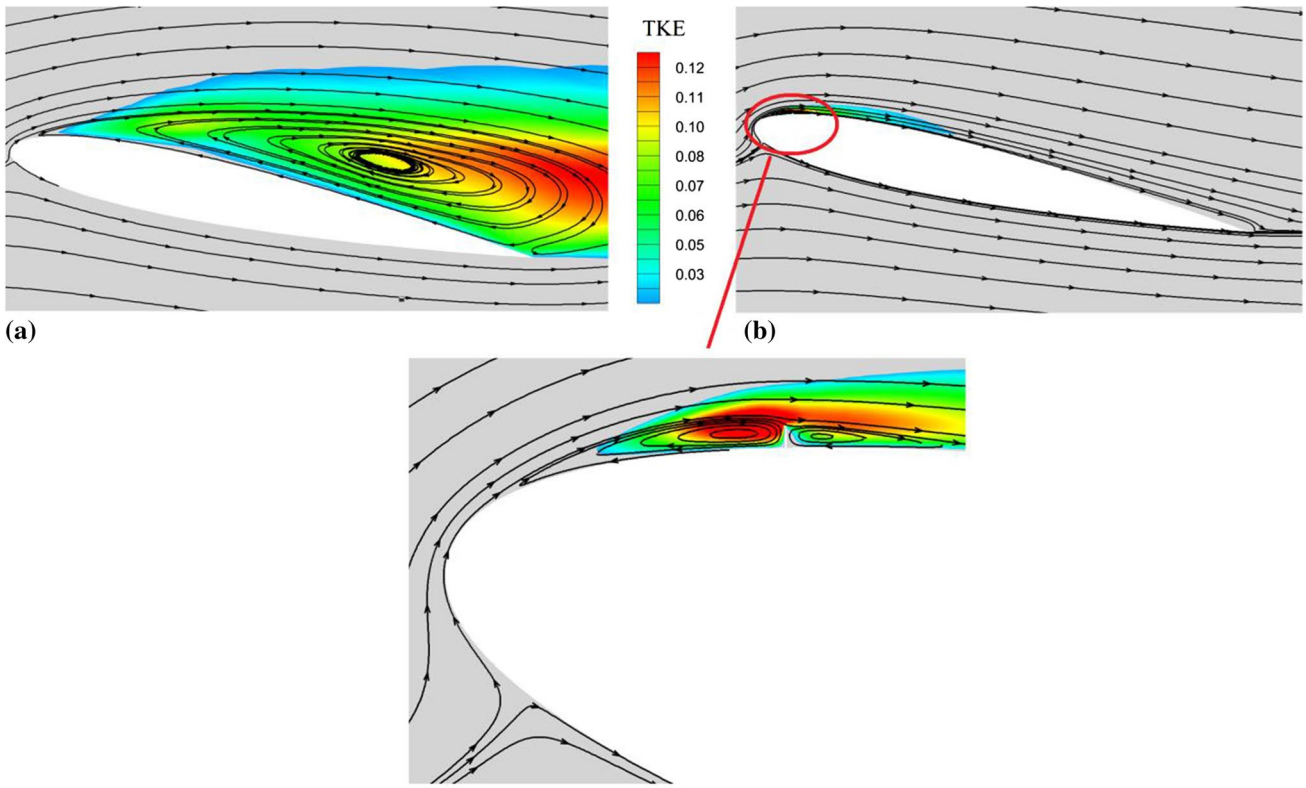

Fig. 11 Contours and streamlines of the turbulent kinetic energy at $\alpha = 12°$, **a** baseline airfoil **b** bladed airfoil

Table 1 Pitching characteristics of the airfoils

	Case 1	Case 2	Case 3	Case 4	Case 5
α_m (deg.)	10	10	10	10	10
α_0 (deg.)	5	5	5	10	10
K	0.05	0.1	0.15	0.1	0.2

it is found that the blade causes a delay in the flow separation onset. This fact can be observed in the drag coefficient curves because the flow separation increases the drag coefficient with a great slope. In the cases of 1–3 (Figs. 12, 13 and 14), as the reduced frequency increases, the dynamic stall effect on the aerodynamic coefficients of the baseline airfoil increases, while on the bladed airfoil decreases. In other words, the blade leads to an improved aerodynamic performance for the airfoil at higher frequencies. It can be argued that the increase in the oscillation frequency leads to the development of the turbulence in the flow field that reduces the growth of the vortices. In the cases of 4 and 5 (Figs. 15 and 16), the angular amplitude increases from 5° to 10°. The results are similar to the previous cases except that the effect of the blade on the dynamic stall suppression is reduced because as the angle of attack range increases, the strength of the vortices increases. In these two cases, the fluctuations resulting from the blade are not able to supply the sufficient

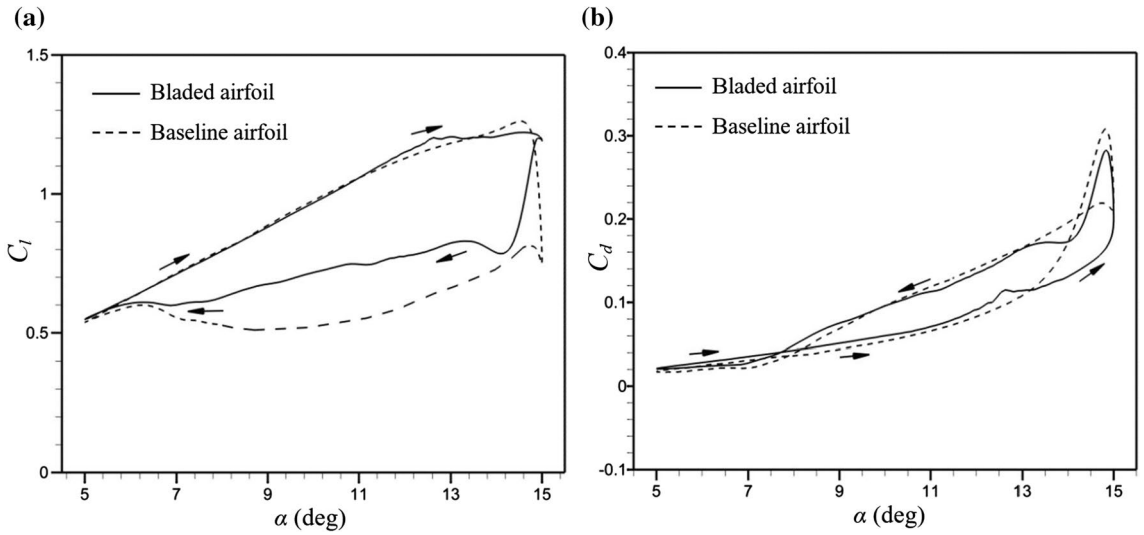

Fig. 12 Comparison of the aerodynamic coefficients for the baseline and bladed NACA 0012 airfoils, $\alpha_m = 10°$, $\alpha_0 = 5°$, $k = 0.05$, **a** C_l, **b** C_d

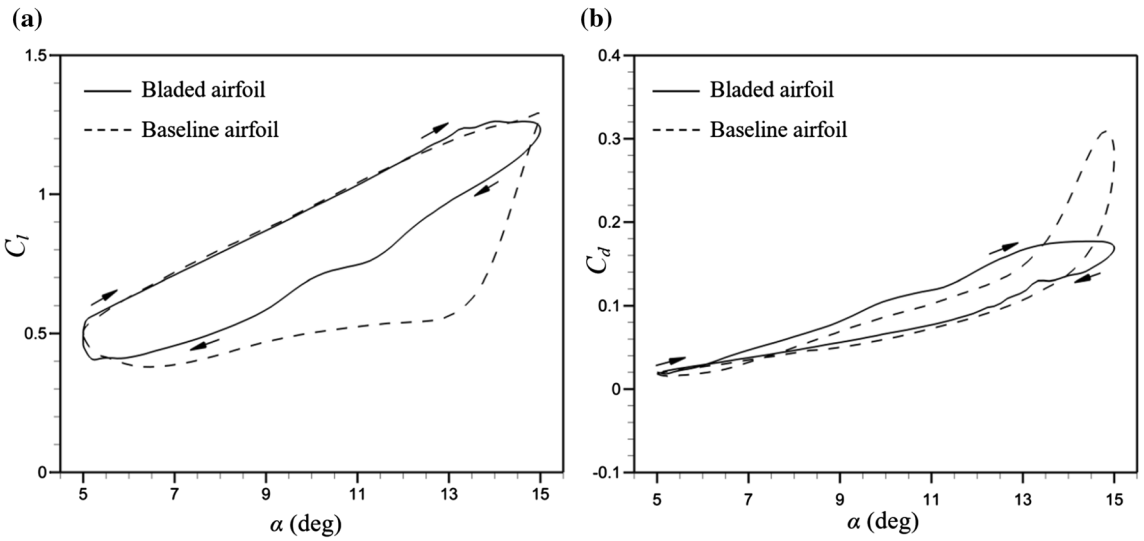

Fig. 13 Comparison of the aerodynamic coefficients for the baseline and bladed NACA 0012 airfoils, $\alpha_m = 10°$, $\alpha_0 = 5°$, $k = 0.1$, **a** C_l, **b** C_d

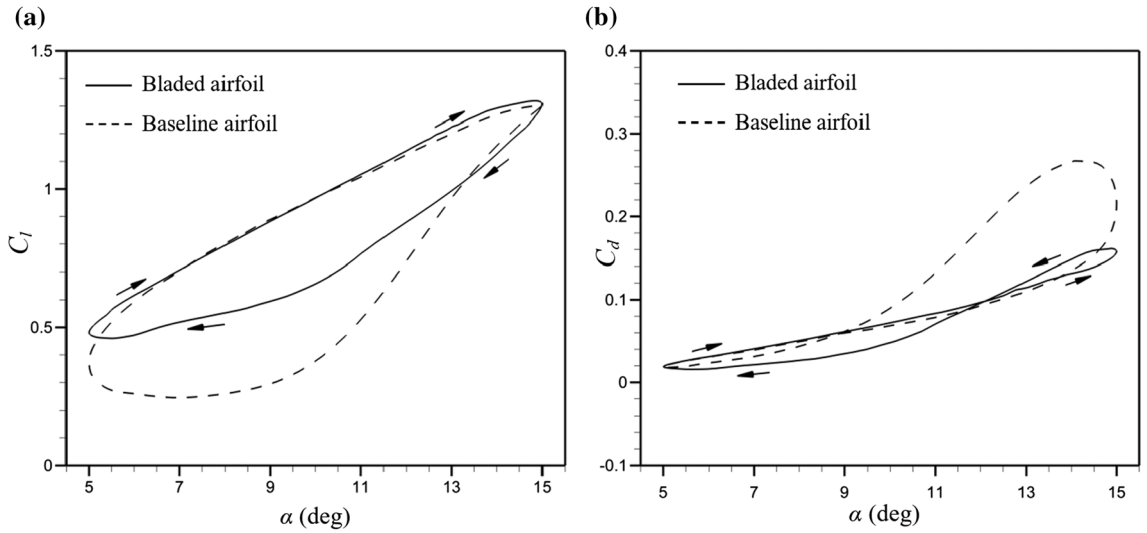

Fig. 14 Comparison of the aerodynamic coefficients for the baseline and bladed NACA 0012 airfoils, $\alpha_m = 10°$, $\alpha_0 = 5°$, $k = 0.15$, **a** C_l, **b** C_d

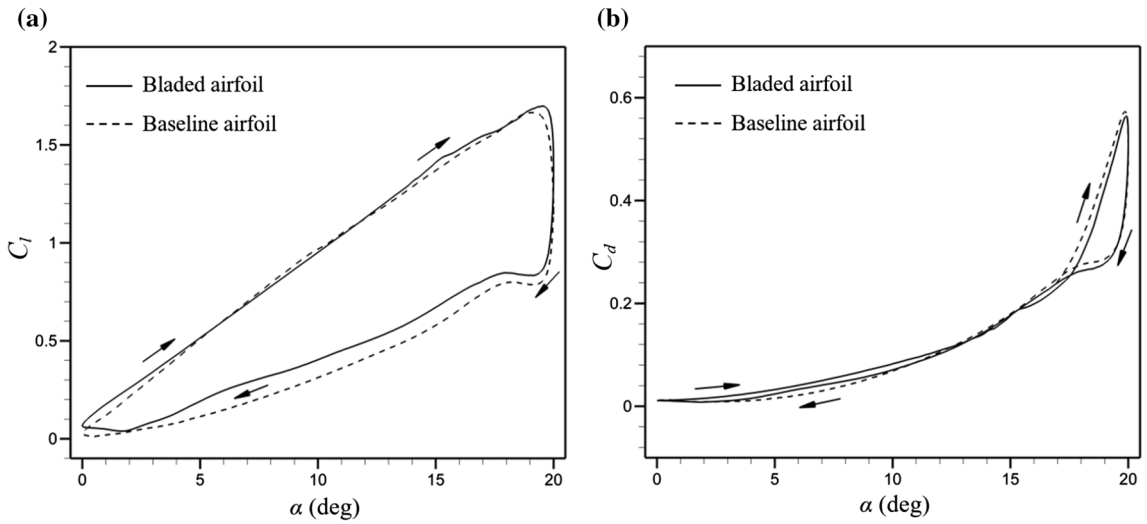

Fig. 15 Comparison of the aerodynamic coefficients for the baseline and bladed NACA 0012 airfoils, $\alpha_m = 10°$, $\alpha_0 = 10°$, $k = 0.1$, **a** C_l, **b** C_d

momentum to overcome the vortices. On the other hand, by increasing the blade height, the aerodynamic performance of the airfoil is not expected to improve; because according to Fig. 11, a vortex is formed in front of the blade. As the blade height increases, the vortex becomes larger, which reduces the suction peak on the leading edge.

Figure 17 shows the streamlines along with the turbulent kinetic energy contours of the baseline and bladed airfoils for Case 3 ($\alpha_m = 10°$, $\alpha_0 = 5°$, $k = 0.15$) at four angles of attack. At $\alpha = 5°$, the flow is separated for the baseline airfoil almost on the middle of the upper surface, while for the bladed airfoil, a separation bubble is observed on the leading edge. By comparing the TKE contours, it can be found that the blade makes the turbulence stronger than the baseline airfoil and moves it to the leading edge due to the local pressure changes. At $\alpha = 10°$ (pitch up motion), a similar separation bubble is seen on both of the airfoils, although there is more turbulence on the bladed airfoil's surface than on the baseline airfoil's one. At $\alpha = 15°$, further turbulence on the bladed airfoil leading edge increases the Reynolds stresses and, therefore, significantly prevents the bubble from growing. For the baseline airfoil, the growing bubble is observed. At $\alpha = 10°$ (pitch down motion), the flow turbulence on the upper surface of the baseline airfoil decreases. A long separation bubble covers the entire surface leading to a severe decrease and increase in the lift and drag coefficients, respectively. There is more

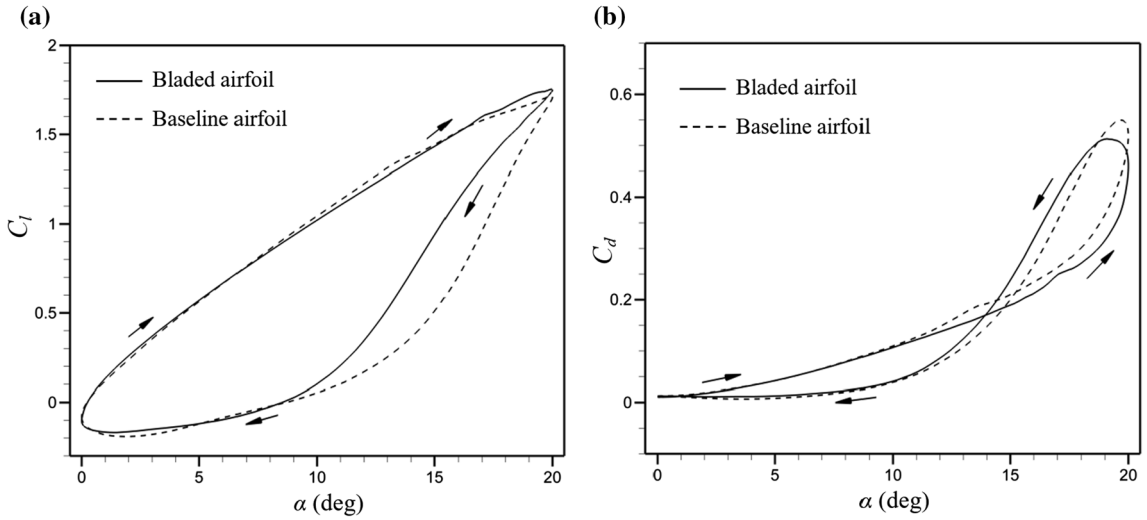

Fig. 16 Comparison of the aerodynamic coefficients for the baseline and bladed NACA 0012 airfoils, $\alpha_m = 10°$, $\alpha_0 = 10°$, $k = 0.2$, **a** C_l, **b** C_d

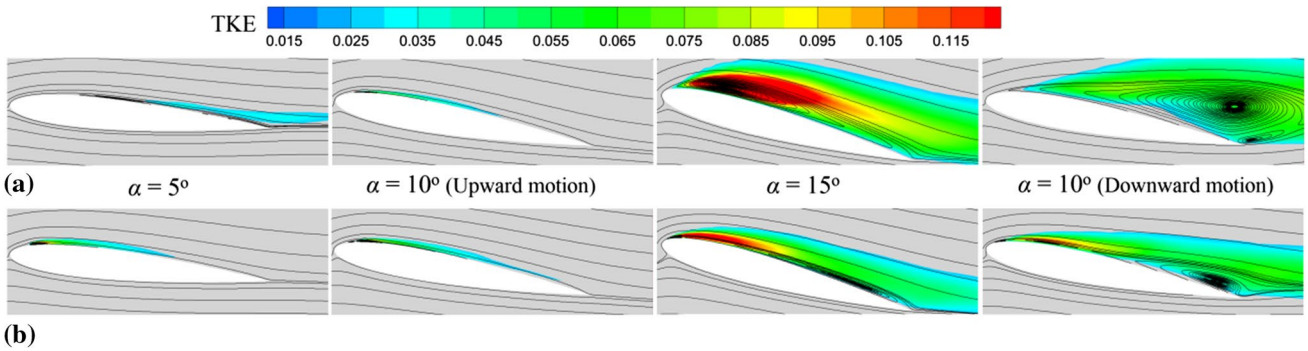

Fig. 17 Streamlines and TKE contours of Case 3 ($\alpha_m = 10°$, $\alpha_0 = 5°$, $k = 0.15$) at four angles of attack, (a) baseline airfoil (b) bladed airfoil

turbulence on the bladed airfoil, which causes another separation bubble to form on the surface.

4 Conclusions

In this paper, the effect of a bubble burst control blade on the dynamic stall suppression of the NACA 0012 airfoil at different angular amplitudes and frequencies was numerically analyzed at $\mathrm{Re} = 1.3 \times 10^5$. An in-house second-order finite-volume solver was developed to compute the flow field. An appropriate version of the k-k_L-ω turbulence model was utilized to capture the laminar separation bubble. The blade was located normal to the airfoil surface on the 0.07 chord from the leading edge with a height of 0.005 chord length. The stationary airfoil results showed that the bubble burst control blade increased the static stall angle from 12° to 13°. For the pitching airfoil, the blade caused a delay in the onset of the flow separation and improved the lift and drag coefficients in the pitch down motion of the airfoil. The turbulent kinetic energy contours indicated that the blade made the turbulence stronger than the baseline airfoil and moved it toward the leading edge. As the oscillation frequency increased, the dynamic stall depth in the bladed airfoil decreased. The best improvement was at the angular amplitude of 5° and reduced frequency of 0.15. At the higher angular amplitude of 10°, the blade performance decreased because of a growth in the vortex strength. The advantage of the applied mechanism over other mechanisms is that it can be easily and cheaply installed on all types of airfoils.

References

1. Abbasi A, Yazdani S (2021) A numerical investigation of synthetic jet effect on dynamic stall control of oscillating airfoil. Scientia Iranica 28:343–354
2. Abdelraouf H, Elmekawy AMN, Kassab SZ (2020) Simulations of flow separation control numerically using different plasma actuator models. Alex Eng J 59:3881–3896

3. Akbari MH, Price SJ (2003) Simulation of dynamic stall for a NACA 0012 airfoil using a vortex method. J Fluids Struct 17:855–874
4. Alferez N, Mary I, Lamballais E (2013) Study of stall development around an airfoil by means of high fidelity large eddy simulation. Flow Turbul Combust 91:623–641
5. Almutairi J, Eljack E, Alqadi I (2017) Dynamics of laminar separation bubble over NACA-0012 airfoil near stall conditions. Aerosp Sci Technol 68:193–203
6. Bak khoshnevis A, Yazdani S, Salimipour E (2020) Effects of CFJ flow control on aerodynamic performance of symmetric NACA airfoils. J Turbulence 21:704–721
7. Benton SI, Visbal MR (2018) Effects of leading-edge geometry on the onset of dynamic stall. AIAA J 56:4195–4198
8. Carmichael BH (1981) Low reynolds number airfoil survey
9. Carr LW (1988) Progress in analysis and prediction of dynamic stall. J Aircr 25:6–17
10. Choudhuri PG, Knight DD, Visbal MR (1994) Two-dimensional unsteady leading-edge separation on a pitching airfoil. AIAA J 32:673–681
11. Costes M, Richez F, le Pape A, Gavériaux R (2015) Numerical investigation of three-dimensional effects during dynamic stall. Aerosp Sci Technol 47:216–237
12. Garmann DJ, Visbal MR (2011) Numerical investigation of transitional flow over a rapidly pitching plate. Phys Fluids 23:094106
13. He G, Deparday J, Siegel L, Henning A, Mulleners K (2020) Stall delay and leading-edge suction for a pitching airfoil with trailing-edge flap. AIAA J 58:5146–5155
14. Kan Z, Li D, Zhao S, Xiang J, Sha E (2021) Aeroacoustic and aerodynamic characteristics of a morphing airfoil. Aircraft Eng Aerosp Technol
15. Kaufmann K, Merz C, Gardner AD (2016) Dynamic stall simulations on a pitching finite wing. In: 34th AIAA applied aerodynamics conference
16. Khoshnevis A, Yazdani S, Saimipour E (2020) Analysis of co-flow jet effects on airfoil at moderate Reynolds numbers. J Theor Appl Mech 58:685–695
17. Lee T, Gerontakos P (2004) Investigation of flow over an oscillating airfoil. J Fluid Mech 512:313–341
18. Magill J, Bachmann M, Rixon G (2003) Dynamic stall control using a model-based observer. J Aircr 40:355–362
19. Marxen O, Henningson D (2008) Direct numerical simulation of a short laminar separation bubble and early stages of the bursting process. New Results in Numerical and Experimental Fluid Mechanics VI
20. Mccroskey WJ (1982) Unsteady Airfoils. Ann Rev Fluid Mech 14:285–311
21. Miotto R, Wolf W, Gaitonde D, Visbal M (2022) Analysis of the onset and evolution of a dynamic stall vortex on a periodic plunging aerofoil. J Fluid Mech, 938
22. Mishra A, Kumar G, De A (2019) Prediction of separation induced transition on thick airfoil using non-linear URANS based turbulence model. J Mech Sci Technol 33:2169–2180
23. Nived M, Mukesh BS, Athkuri SSC, Eswaran V (2021) On the performance of RANS turbulence models in predicting static stall over airfoils at high Reynolds numbers. International J Numer Methods Heat Fluid Flow
24. Patial S, Jain P, Rawat P, Bodavula A, Yadav R (2020) The study of the effect of the cavity on the flow over NACA 0012 and SELIG 7003 aerofoil at low Reynolds number using vortex shading method. AIAA Scitech 2020 forum
25. Rarata Z (2021) The effect of wavy surface on boundary layer instabilities of an airfoil. Aircraft Eng Aerosp Technol
26. Rinoie K, Okuno M, Sunada Y (2009) Airfoil stall suppression by use of a bubble burst control plate. AIAA J 47:322–330
27. Salimipour E (2019a) A modification of the k-kL-ω turbulence model for simulation of short and long separation bubbles. Comput Fluids 181:67–76
28. Salimipour E (2019b) A numerical study on the fluid flow and heat transfer from a horizontal circular cylinder under mixed convection. Int J Heat Mass Transfer 131:365–374
29. Salimipour E, Salimipour A (2019) Power minimization and vortex shedding elimination of a circular cylinder by moving surface mechanism. Ocean Eng 189:106408
30. Salimipour E, Yazdani S (2020) Improvement of aerodynamic performance of an offshore wind turbine blade by moving surface mechanism. Ocean Eng 195:106710
31. Salimipour E, Yazdani S, Ghalambaz M (2021) Flow field analysis of an elliptical moving belt in transitional flow regime. Eur Phys J Plus 136:783
32. Salimipour SE, Teymourtash AR, Mamourian M (2018) Investigation and comparison of performance of some air gun projectiles with nose shape modifications. In: Proceedings of the Institution of Mechanical Engineers, Part P: Journal of Sports Engineering and Technology, 233, 3-15
33. Samson A, Sarkar S (2015) An experimental investigation of a laminar separation bubble on the leading-edge of a modelled aerofoil for different reynolds numbers. Proc Inst Mech Eng C J Mech Eng Sci 230:2208–2224
34. Sandham ND (2016) Transitional separation bubbles and unsteady aspects of aerofoil stall. Aeronaut J 112:395–404
35. Tani I (1964) Low-speed flows involving bubble separations. Progress Aeros Sci 5:70–103
36. Visbal MR (2014) Analysis of the onset of dynamic stall using high-fidelity large-eddy simulations. In: 52nd aerospace sciences meeting
37. Visbal MR, Benton SI (2018) Exploration of high-frequency control of dynamic stall using large-eddy simulations. AIAA J 56:2974–2991
38. Visbal MR, Garmann DJ (2018) Analysis of dynamic stall on a pitching airfoil using high-fidelity large-eddy simulations. AIAA J 56:46–63
39. Visbal MR, Garmann DJ (2020) Mitigation of dynamic stall over a pitching finite wing using high-frequency actuation. AIAA J 58:6–15
40. Walters DK, Cokljat D (2008) A three-equation eddy-viscosity model for reynolds-averaged navier–stokes simulations of transitional flow. J Fluids Eng, 130
41. Wang H, Jiang X, Chao Y, Li Q, Li M, Zheng W, Chen T (2019) Effects of leading edge slat on flow separation and aerodynamic performance of wind turbine. Energy 182:988–998
42. Wang H, Zhang B, Qiu Q, Xu X (2017) Flow control on the NREL S809 wind turbine airfoil using vortex generators. Energy 118:1210–1221
43. Zhang Y, Zhou Z, Wang K, Li X (2020) Aerodynamic characteristics of different airfoils under varied turbulence intensities at low reynolds numbers. Appl Sci 10:1706